Static hydroelastic study of composite T-foils with beam and lifting line models

Galen W. Ng[1,*], Eirikur Jonsson[2], Yingqian Liao[3], Sicheng He[4], Joaquim R.R.A. Martins[5]

ABSTRACT

Well-designed hydrofoils improve ship resistance and seakeeping by lifting the hull above the water. With greater speeds come greater loads, and the two-way interaction of structural deflections of lifting surfaces on the hydrodynamics must be considered. Tailored structural anisotropy can improve hydrodynamic and structural efficiency of lifting surfaces compared to rigid counterparts by exploiting the layup of composite materials. Structural efficiency here means reduced risk of structural failure for a given amount of material, and hydrodynamic efficiency means lower drag. A T-foil is a prototypical multi-component appendage, consisting of the foil wing and the strut, which we investigate in this work. We use simple composite beam and lifting line theory to explore the static fluid-structure interaction of a composite T-foil for a variety of fiber angles ($\theta_f = 0°, \pm15°$). We apply a simple approximation on lift coefficient at infinite Froude number (Fn) to model the free-surface effects, which is valid at high depth-based Froude numbers ($Fn_h > 10\sqrt{h/c}$) when C_L is independent of Fn_h and the inertial effects dominate. Results for the moth rudder T-foil geometry studied here indicate that aligning composite fibers towards the leading edge results in a more hydrostructurally efficient foil and that free-surface effects are minor because of the large submergence for this flow condition.

KEY WORDS

Hydrodynamics; Composite structures; Hydrofoil; Hydroelasticity; Fluid-structure interaction

INTRODUCTION

T-foils are prototypical lifting surface configurations commonly used to lift a vessel above the free surface. Flying above the water improves seakeeping performance because of the reduced waterplane area. Foiling also removes any resistance associated with hullborne operation: hull wetted skin friction drag, hull form drag, hull wave making drag, wave added resistance, etcetera. For a fixed amount of total resistance, a foiling vessel can sail much faster than a hullborne one since drag force scales with speed squared. In other words, foilborne vessels have better energy efficiency than hullborne vessels in higher speed regimes, which was investigated by Godø and Steen (2023a). However, faster vessels come with concerns for cavitation and ventilation phenomena on the foils. Additionally, loads on the structure approach yield limits, and the two-way coupled effect of the deformed state of the foils on the hydrodynamic loads must also be considered. Hydroelastic analysis is thus critical for the accurate assessment of higher speed vessels.

[1] Ph.D. Candidate (University of Michigan, Ann Arbor, USA); ORCID: 0000-0001-7980-9483
[2] Post-doctoral research fellow (University of Michigan, Ann Arbor, USA); ORCID: 0000-0002-5166-3889
[3] Post-doctoral research fellow (University of Michigan, Ann Arbor, USA); ORCID: 0000-0001-6904-8844
[4] Assistant Professor (University of Tennessee, Knoxville, USA); ORCID: 0000-0003-1307-4909
[5] Pauline M. Sherman Collegiate Professor (University of Michigan, Ann Arbor, USA); ORCID: 0000-0003-2143-1478
[*] Corresponding Author: Galen W. Ng nggw@umich.edu

More recently, composite materials have gained the interest of foil designers because of hydroelastic tailoring, which improves the hydrodynamic and structural performance of these devices in off-design conditions. Directional stiffness, or *material anisotropy* opens up the potential for passive, load-dependent, shape-adaptative marine structures. A more structurally efficient foil can be realized because deflections under fluid load can be designed to avoid critical stresses and deflections, and hence material failure. Flow-induced vibrations and noise can also be designed away through tuning of plies and structural sizing variables (Ng et al., 2022; Mulcahy et al., 2014; Groo et al., 2019). These structurally efficient foils require less material to achieve a given objective. Composites also improve hydrodynamic efficiency through lower drag designs because the load-dependent deflections favorably reduce subcavitating drag as demonstrated by Liao et al. (2021).

The composite structure can be modeled with varying fidelity to capture quantities of interest. For example, Faye et al. (2024) used low-fidelity composite beam elements to model material bend-twist coupling for a deflecting hydrofoil. Beam theory is cheap, but it can miss some material failure mechanisms. In contrast, Liao et al. (2023) modeled grouped layers of composite laminates with brick finite element models of a hydrofoil to more accurately capture through-thickness stresses and deformations that can then be used in more rigorous material failure criteria. Maung et al. (2023) went further with their composite hydrofoil optimization using a detailed finite element model of a hydrofoil with curved fibers that also captured ply drops.

For lifting surfaces operating near the free surface, one must additionally consider the effects of free-surface proximity on the loads and local pressures on the appendage to accurately optimize a design. The first-order effects of the free surface boundary on hydrodynamic loads can mostly be captured with potential flow methods and a linearized free-surface boundary condition. A numerical lifting line method is the lowest order potential flow model appropriate for loads on a hydrofoil wing. Godø and Steen (2023b) present one example of a lifting line method for determining the hydrodynamic loads on a hydrofoil with linearized free-surface effects computed through a Green's function, which avoids the need to mesh the free surface boundary. Nicolas et al. (2023) used the linearized free-surface boundary condition as well but modeled the hydrofoil with panels on the body, which captures thickness and lifting effects more accurately than a lifting line method. Beck and Reed (2001, Fig. 1) presents an overview of numerical methods for handling free surface effects from inviscid potential flow to viscous direct numerical simulation. The latter is too costly for preliminary design and analysis, which is the area of focus for this work.

At low speeds, the free surface behaves like a rigid wall boundary, whereas at high speeds, it acts as pressure relief because the perturbations forces of the moving body overcome the gravity of the water that maintains the rigid wall behavior at low speeds (Faltinsen, 2006, Ch. 6). The non-dimensional number that best characterizes these regimes of free-surface effects is the *Froude number*, which is the ratio of inertial to gravitational forces. The chord-based (c) and depth-based (h) Froude numbers are given by

$$Fn_c = \frac{U_\infty}{\sqrt{gc}}, \qquad Fn_h = \frac{U_\infty}{\sqrt{gh}}. \tag{1}$$

Faltinsen (2006, Ch. 6) presents approximations to the hydrodynamics loads in the Froude number limits used in this work.

The choice of hydrodynamic and structural model fidelity depends on the balance between computational speed and required accuracy of the physics to assess a candidate design. This work deals with preliminary hydroelastic design of foils so we deem lifting line and composite beam theories as adequate. First, we discuss the theoretical background and the case setup of our hydro-structural model in the Dynamic Composite Foil (DCFoil.jl) program. Then, we present and discuss the static hydroelastic behavior of a moth T-foil rudder for various material configurations with the free-surface effect turned on and off. We conclude with overall insights based on our results and suggestions for future work.

METHODOLOGY

The following sections describe the basic background of the static analysis mode of the Dynamic Composite Foil (DCFoil.jl) program. DCFoil.jl was originally developed considering second-order dynamical system analysis in the mass-

spring-dashpot sense of $\mathbf{M_s\ddot{u}} + \mathbf{C_s\dot{u}} + \mathbf{K_s u} = \mathbf{f_{hydro}}$ (Ng et al., 2023), but we remove time derivative terms for static analysis. The governing discrete equation for static analysis is

$$\mathbf{K_s u} = \underbrace{\mathbf{f}_{\mathrm{hydro}}(\mathbf{u})}_{=-(\mathbf{K_f})\mathbf{u}} \tag{2}$$

where $\mathbf{u}$ are the structural states, $\mathbf{K_s}$ is the structural stiffness matrix, and $\mathbf{K_f}$ is the hydrodynamic stiffness matrix. We solve this equation for $\mathbf{u}$ using a Newton-Raphson scheme. The next section describes the computation of $\mathbf{K_s}$; the following, $\mathbf{K_f}$. The global coordinate system, shown in Figure 1, is x streamwise, y to starboard, and z up.
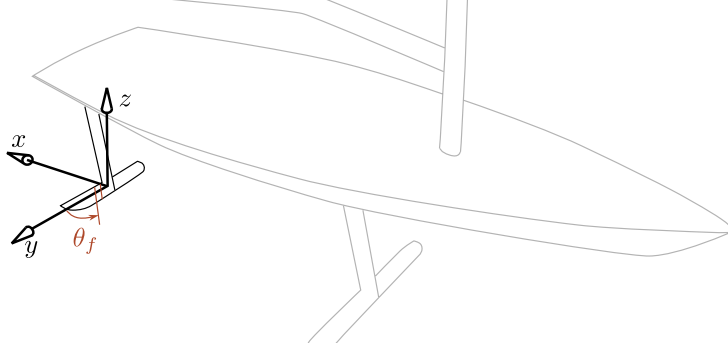

Figure 1: Global coordinate system for the composite T-foil with positive fiber angle convention.

Composite beam finite element model

The composite beam model has been previously developed and validated against a composite plate model in ABAQUS (Ng et al., 2023). The beam finite element has two nodes with nine degrees of freedom at each node to account for structural warping. The only noteworthy new extension to the implementation is the mesh generation routine for a T-foil. Previously, we only studied cantilevered beams (half-wing). We updated the routine for generating meshing and element connectivity to handle three "half-wings": two port-starboard (P/S) symmetric wings and one strut. Figure 2 shows the stick model.

As for structural properties, we specify only two sets of parameters for the half-wing and strut, since the wings are P/S symmetric. For example, a fiber angle of $\theta_f = 15°$ on the starboard wing (aligned towards the leading edge) is mirrored on the port wing. We assume the elastic axis (locus of shear centers) is along the midchord.

Hydrodynamic lifting line model

The basic lifting line model builds on our previous work (Ng et al., 2022, 2023) that follows Glauert's method (Glauert, 1983, Ch. 11) for the static lifting line of a hydrofoil of arbitrary planform. We assume a Fourier sine series expansion for the spanwise vorticity $\gamma(y)$ and solve a linear system for the Fourier coefficients using relations for the spanwise downwash and vorticity. Because the strut interrupts the wing at the centerline, the spanwise vorticity is zeroed out at the junction collocation node. Then we compute the spanwise lift slope $c_{\ell_\alpha}(y)$ to populate the $\mathbf{K_f}$ matrix. The center of lift is at $c/4$ for each section, which is an inviscid thin-airfoil assumption. Note, the quarter-chord center of pressure assumption does lose validity at higher angles of attack because of flow separation that causes the center of pressure to migrate towards the midchord.

In steady-state potential flow, the *negative image method* is appropriate for representing the free surface in the high Froude number limit. Conversely, the *positive image method* is for low Froude number flows. The *linearized*[1] *free-surface bound-*

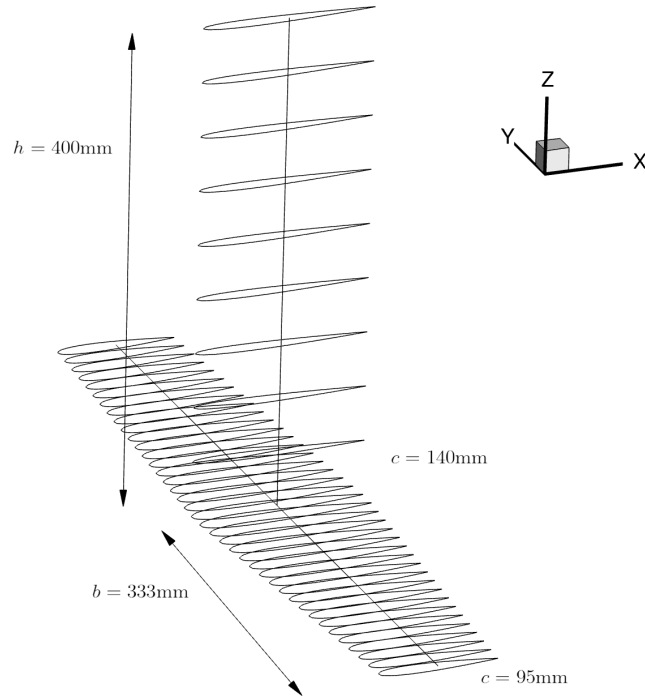[1] Assuming small wave slopes and removing higher order velocity terms

Figure 2: Stick model of a T-foil with overall dimensions labeled. Airfoil slices are drawn at node locations to aid with visualization.

ary condition, which can be derived from combining a dynamic and kinematic boundary condition (Newman, 2018, Sec. 6.1), is

$$U_\infty^2 \frac{\partial^2 \varphi}{\partial x^2} + g \frac{\partial \varphi}{\partial z} = 0 \quad \text{for } z = 0, \tag{3}$$

where $z = 0$ is the mean free surface and φ is the perturbation potential of the lifting body. The total potential is $\Phi = U_\infty x + \varphi$. Equation 3 tells us the first term vanishes for low Fn, and the second term vanishes for high Fn. For high Froude numbers, $\varphi = 0$ on $z = 0$ is a solution to the boundary condition equation 3. Putting negative images of source and vortex singularities equal distances from the free surface as the actual body satisfies this. Approximations to the asymptotical behavior of lift and drag at high Froude numbers exist that facilitate rapid analysis for submerged lifting surfaces. Faltinsen (2006) gives this 2D lift relation accounting for free-surface effect

$$c_\ell \left(\frac{h}{c} \right) = c_\ell \left(\frac{h}{c} = \infty \right) \cdot \left[\frac{1 + 16(h/c(y))^2}{2 + 16(h/c(y))^2} \right] \quad \text{for } Fn_h > 10/\sqrt{h/c}, \tag{4}$$

where the bracketed term is a "corrective" factor accounting for the negative image vortex. The extension to a 3D foil follows as a correction on the spanwise vorticity. The spanwise vorticity, is a decomposition of circulation in 2D and downwash-induced circulation from neighboring vortex elements

$$\gamma(y) = \underbrace{\gamma_{2D}}_{\text{airfoil}} \underbrace{-\pi c(y) w_i(y)}_{\text{downwash effect}}. \tag{5}$$

The correction applies to the airfoil vorticity

$$\gamma_{2D}\left(y, \frac{h}{c}\right) = \underbrace{-U_\infty c(y)\pi\alpha}_{\gamma_{2D}\left(y, \frac{h}{c}=\infty\right)} \left[\frac{1 + 16(h/c)^2}{2 + 16(h/c)^2}\right]. \tag{6}$$

We compute the total spanwise vortex strength $\gamma(y)$ from Glauert's method so we simply subtract the γ_{2D} with no free-surface effect and add back the circulation with free-surface effect (Equation 6).

CASE SETUP

The T-foil model is based on the moth rudder T-foil studied by Liao et al. (2022); Ashworth Briggs (2018); Binns et al. (2008). The foil has a 0.4 m strut with a NACA0015 section. The wings are NACA0012 sections with a $b = 0.333$ m semis-pan, a root chord of 0.14 m, and a tip chord of 0.095 m. The stick model showing the dimensions is given in Figure 2. We use 19 elements for each half wing and nine for the strut. The planform area of a half-wing is 0.039m^2, and the area we use in nondimensionalization of forces in the next section is twice that value ($A = 0.078\text{m}^2$).

The material properties are for uni-directional (UD) carbon fiber-reinforced plastic (CFRP) given in Table 1. In reality, the foil would be made of a laminate with several plies of different angles embedded in a resin matrix to avoid crack propagation, but for the purposes of exploring anisotropy effects, these mechanical properties are adequate.

Table 1: Subscript 1 is along the fiber, 2 is in-plane, and 3 is out-of-plane.

Variable	Symbol	CFRP	Units
Solid density	ρ_s	1,590	kg/m³
Elastic moduli	E_1	117.8	GPa
—	$E_2 = E_3$	13.4	GPa
Shear moduli	$G_{12} = G_{23}$	3.9	GPa
Poisson's ratio	$\nu_{12} = \nu_{13}$	0.25	—

For the flow setup, we consider one speed of $U_\infty = 18$ m/s (≈ 35 kts), which corresponds to the top speed analyzed by Liao et al. (2022) and is consistent with typical hull speeds sailorscan achieve during races. The depth Froude number is then $Fn_h = 9.09$, which is greater than the highest limiting value of $10/\sqrt{h/c} = 5.92$ at the root chord, so the negative image method applies. Fluid density is $\rho_f = 1025$ kg/m³ for seawater. We assume no yaw angle or leeway effects, so flow comes head on and the strut produces no load. The wing has a base rake angle of $\alpha_r = 2°$.

We look at three hydrofoils with varying fiber angles on the wing. The first is $\theta_f = 0°$ and the next two are $\pm 15°$. The strut fiber angle stays at $\theta_f = 0°$ because there will be no side loads in these cases. We also divide the results further into the ones with a deeply submerged assumption (no correction to $\gamma(y)$) and ones with the free surface model as explained prior. The foils will not all produce the same lift, so at the end, we run a polar varying α_r.

RESULTS

The following section first discusses the case setup and then presents the results.

Static hydroelasticity of the T-foils

Lifting forces and deflections

In Table 2, we see the lift generated by the various foils. As one would expect, as fiber angle goes from negative to positive (trailing edge to leading edge), the total lift decreases because of an increased de-pitching effect to which the material anisotropy contributes. Furthermore, the lift between no free surface model and the free surface model decreases marginally because of the reduction in circulation caused by proximity to the free surface at high Fn_h. The reduction is minor because depth-to-chord ratio (h/c) is high. The depth-to-chord ratio is squared in Equation (6) and thus brings the correction factor close to unity. The reduction in forces is also less pronounced when less lift is produced.

Table 2: Lift of the various foils with percent difference from no free surface model.

	$\theta_f = -15°$		$\theta_f = 0°$		$\theta_f = 15°$	
	L [N]	C_L	L [N]	C_L	L [N]	C_L
No free surface model	5738.7	0.442	2469	0.190	1787	0.138
Free surface model	5527.9 (-3.7%)	0.425	2444 (-1.0%)	0.188	1776 (-0.6%)	0.137

Table 3 presents the moments about the midchord where positive is nose-up. Consistent with the lift trend, the moments also decrease as the fiber angle goes from negative to positive angle alignment. The percentage difference between free sur-

Table 3: Moment about midchord line of the various foils.

	$\theta_f = -15°$		$\theta_f = 0°$		$\theta_f = 15°$	
	M_y [N-m]	C_{My}	M_y [N-m]	C_{My}	M_y [N-m]	C_{My}
No free surface model	165.1	0.108	73.2	0.048	54.0	0.035
Free surface model	159.2 (-3.6%)	0.104	72.5 (-1.0%)	0.047	53.7 (-0.6%)	0.035

face and no free surface model are also consistent with lift trends, since the differences are smaller for more lightly loaded foils. The overall moments remain positive because the center of lift (assumed $1/4$ chord) are all upstream of the midchord location. Moments decrease because there is less lift applied.

The total lift loads and coefficients are consistent with Reynolds-averaged Navier-Stokes (RANS) simulations by Liao et al. (2022) as these foils are also around $C_L = 0.2$ except for the $\theta_f = -15°$ foil, which produces much more lift. We would not expect identical loads since the foils are not identical to Liao et al. (2022), and we have structural compliance in the current study. Furthermore, Liao et al. (2022) used a symmetry boundary condition, which is analogous to the positive image method, so we would expect their results to have slightly more lift than the present study if everything else were the same.

The deflected states of the hydrofoils with no free-surface effect are visualized in Figure 3. The deflections are scaled by two to better visualize the differences between the different fiber angle foils. The $\theta_f = -15°$ T-foil experiences significantly more deflection.

Figure 4 shows the half-wing spanwise loading and deflections for the three fiber angles with no free-surface effect in solid lines and with free-surface effect in dashed lines. There are minor differences, which makes sense because this is a relatively high h/c. At lower submersion depths (smaller h/c), we expect there to be a greater reduction in lift and moments because of free-surface proximity, and thus, the wings would deflect less. The spanwise loads and deflections here illustrate the minor impact the free surface proximity has on the foils.

An implication of these lift and deflection studies is on susceptibility to cavitation and ventilation. Cavitation depends on local pressure dropping below the saturated vapor pressure of water (Brennen, 2014). Ventilation depends on proximity to the free surface, the existence of flow separation, and going above a critical lift threshold (Damley-Strnad et al., 2019;
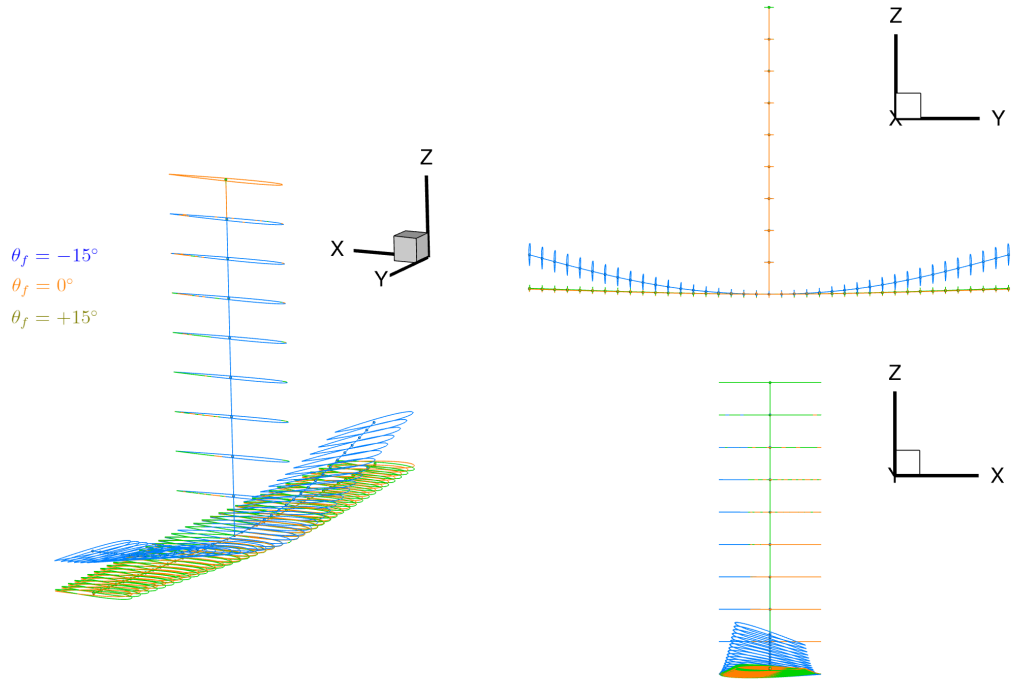
Figure 3: 3D views of the deflected hydrofoil. Deflections scaled by two for visualization purposes.
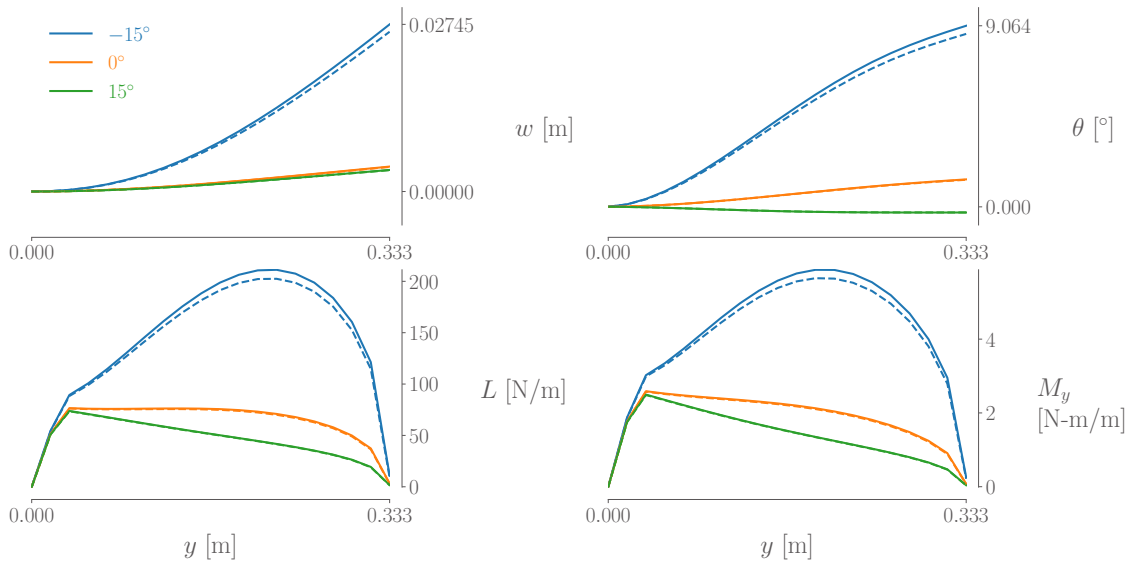

Figure 4: Spanwise vertical bending, twisting, lift, and moment distributions for the different fiber angle T-foils using the deeply submerged assumption (solid) and infinite Froude number free surface effect (dashed).

Young et al., 2017). Based on this intuition, one could deduce that the $\theta_f = -15°$ composite T-foil would have many issues. It produces more lift at the tip than the other foils at this rake angle. The tip twist is around $\theta_{\text{tip}} + \alpha_r = 9° + 2° = 11°$, which when coupled with any variations in angle of attack due to waves or vessel motions could create a strong tip vortex and stall the tip. A strong tip vortex has a low-pressure core, which can result in undesired tip vortex cavitation. Cavitation can be particularly damaging to composite structures (Yamatogi et al., 2009), and it also creates noise and vibrations that

are harmful to the vessel operation. In addition to the cavitation problems, the stalled tip could create a low-energy flow area that is a pathway for air to be sucked down onto the foil. It is also possible for tip vortex cavitation to promote tip ventilation. Collapse of vaporous bubbles induces local velocities towards the body, which break the surface seal earlier than without cavitation. Another effect is that the buoyancy of a cavitating tip vortex is greater than that of a subcavitating tip vortex (Young et al., 2017, Sec. 4.1.4). Sudden ventilation would be detrimental to overall vessel performance and controllability since lift would suddenly drop by about half.

Furthermore, the overall deflections of the $\theta_f = -15°$ hydrofoil are quite high (about 8% of semispan) and structural failure may also be a concern. In contrast, the $0°$ and $15°$ are more well-behaved and safer candidate designs for further exploration because they do not have as high a risk of static structural failure or ventilation. There appears to be little merit to aligning fibers towards the trailing edge unless there were some aileron-like surface outboard, in which case, the controllability of the foiling vessel would be improved. Any dynamic hydroelastic failure mechanisms, such as flutter, remain to be explored.

Drag build-up

A steady-state drag build-up model must consider parasitic drag (D_p) and drag due to lift. Drag due to lift is not the same as lift-induced drag (Kroo, 2001). In equation form, total drag (not considering multiphase flow) is

$$D = D_p + \underbrace{\frac{L^2}{q\pi b^2 e}}_{\text{drag due to lift}} \qquad \text{where } D_p = D_{\text{fric}} + D_{\text{form}} + D_{\text{w}} + D_{\text{int}} + D_{\text{spray}}, \tag{7}$$

and e is the Oswald efficiency factor. For this hydrofoil assuming single-phase flow, the parasitic drag (everything that is not drag due to lift) consists of interference (D_{int}), spray (D_{spray}), wave-pattern (D_{w} assumed zero), skin friction (D_{fric}), and form drag (D_{form}). To supplement the equation form of total drag, Figure 5 hierarchically categorizes the drag components and typical nomenclature used to describe calm-water drag.
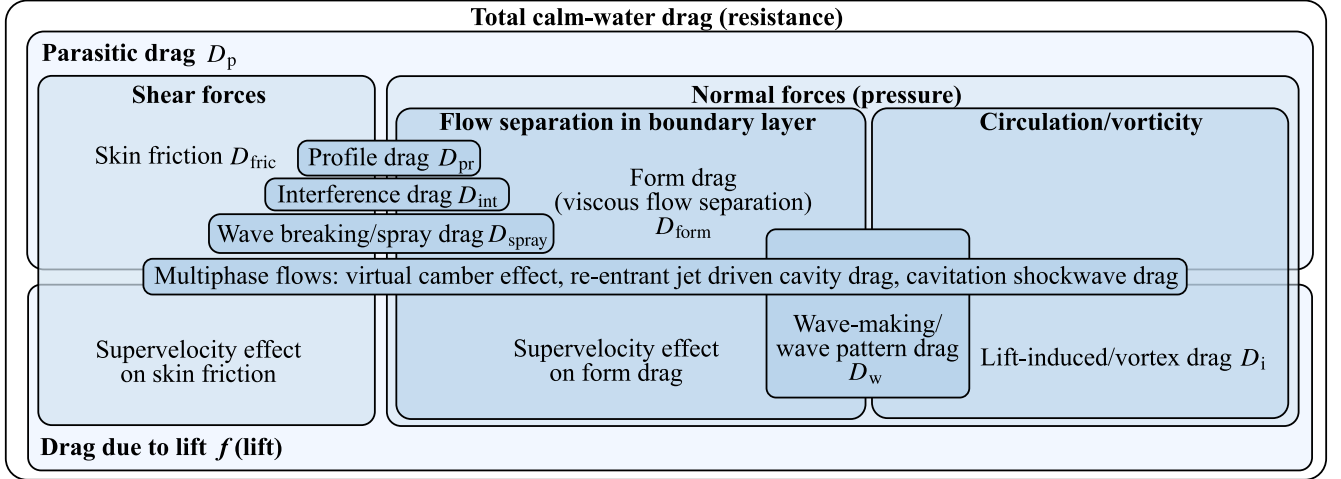

Figure 5: Sources of hydrodynamic drag

A model for the lift-induced drag is based on the spanwise vorticity and downwash. The total induced drag is computed via

$$F_x = -\rho \int_{-b}^{b} \gamma(y) w_i(y) dy \approx -\rho \sum_{n=1}^{\text{nstrips}} \gamma_n(y) w_{i,n}(y) dy_n. \tag{8}$$

The empirical relation for interference drag for a strut junction with no fairing from Hoerner (1965, Ch. 8) is

$$C_{D,\mathrm{j}} = \frac{D_{\mathrm{int}}}{qt^2} = 17\left(\frac{\bar{t}}{c}\right)^2 - 0.05, \tag{9}$$

where $\bar{t}$ is the mean thickness of the strut and wing near the junction and $q = \frac{1}{2}\rho_f U_\infty^2$ is the dynamic pressure. In reality, junction drag depends on much more than the thickness-chord ratio, such as the bluntness of the nose that affects the strength of the necklace vortex (Simpson, 2001).

Due to lifting and thickness effects, the foil generates surface waves, which adds a component called wave drag. The lifting effect on the generated waves tends to be more important. In 2D, wave drag goes to zero at very high Fn_h (Faltinsen, 2006, Ch. 6) and hence we assume it to be zero. In the case of 3D flow, the aforementioned behavior is that of the transverse waves. The divergent waves still contribute to wave drag regardless of how high Fn_h is. It behaves asymptotically at high enough Fn_h, so it would be a constant offset in our results. Nevertheless, we neglect this component due to time constraints, but Faltinsen (2006, Eq. 6.167) gives the relation.

Hoerner (1965, Ch. 10) gave an empirical relation for the spray drag caused by water piling up on the forebody and shooting into the air as $C_{D,\mathrm{s}} = D_{\mathrm{spray}}/(qt_{\mathrm{strut}}^2) = 0.24$, which applies to $Fn_c > 3$. However, this does not consider some details of the strut form, so we use the spray drag relation from Chapman (1971)

$$C_{D,\mathrm{s}} = \frac{D_{\mathrm{spray}}}{qc_{\mathrm{strut}}t_{\mathrm{strut}}} = 0.009 + 0.013\left(\frac{t}{c}\right)_{\mathrm{strut}}, \tag{10}$$

where the location of maximum thickness $(x/c)_{\mathrm{max}}$ is around 35%.

The profile drag (skin friction plus form) at hydrofoil sections assumes a flat-plate estimate with form factor corrections. The friction drag is estimated via the ITTC 1957 line

$$C_f = \frac{D_{\mathrm{fric}}}{q\mathrm{WSA}} = \frac{0.075}{(\log_{10}(Re) - 2.0)^2}, \tag{11}$$

where WSA is wetted surface area. The equation is an empirical formula for skin friction of naked ship hulls assuming turbulent flow (Carlton, 2018). The empirical form factor $(1 + k)$ is determined from Torenbeek (1990) for a subsonic wing

$$1 + k = 1 + 2.7\left(\frac{t}{c}\right) + 100\left(\frac{t}{c}\right)^4, \tag{12}$$

where the first term with thickness captures the increased skin friction from thickness effects and the quartic term accounts for flow separation drag. This equation misses the angle of attack effects on the profile drag, sometimes referred to as a supervelocity effect (Raymer, 2012, Sec. 12.5.5), which increases the skin friction and form drag. Full profile drag is then just $D_{\mathrm{pr}} = (1 + k)D_{\mathrm{fric}}$.

The total drag of the foils at $\alpha_r = 2°$ are in Table 4. Since the foils are not all at the same lift condition, the lift-induced

Table 4: Total drag of the various foils.

| | $\theta_f = -15°$ | | $\theta_f = 0°$ | | $\theta_f = 15°$ | |
	D [N]	C_D	D [N]	C_D	D [N]	C_D
No free surface model	605.7	0.0468	387.3	0.0299	369.4	0.0285
Free surface model	585.2 (-3.4%)	0.0452	386.7 (-0.2%)	0.0299	369.3 (-0.03%)	0.0285

drag plays the biggest role in the differences. The spray and junction drag relations do not depend on lift, so they are identical between the foils. The drag is highest for $\theta_f = -15°$ and decreases for more positive fiber angle since the foils produce less lift. The drag is also reduced when adding free-surface effects because of the reduction in lift. Figure 6 shows the drag build-up for the runs. The results tell the same message that lift-induced drag is the largest contributor to drag differences

between the various foil configurations. Figure 6 also shows that the free surface influences the lift-induced drag calculation for all foils, but the effect is greatest for the foil that produces the most lift ($\theta_f = -15°$). The drag build-up also tells us that profile drag and spray drag are significant portions of total drag that dominate the drag at low C_L conditions; however, this finding is not novel, at least for rigid hydrofoils research. Godø and Steen (2023b) found that strut-related drag, comprised of profile and spray, were large components in total drag (around a quarter of total drag, similar to here).
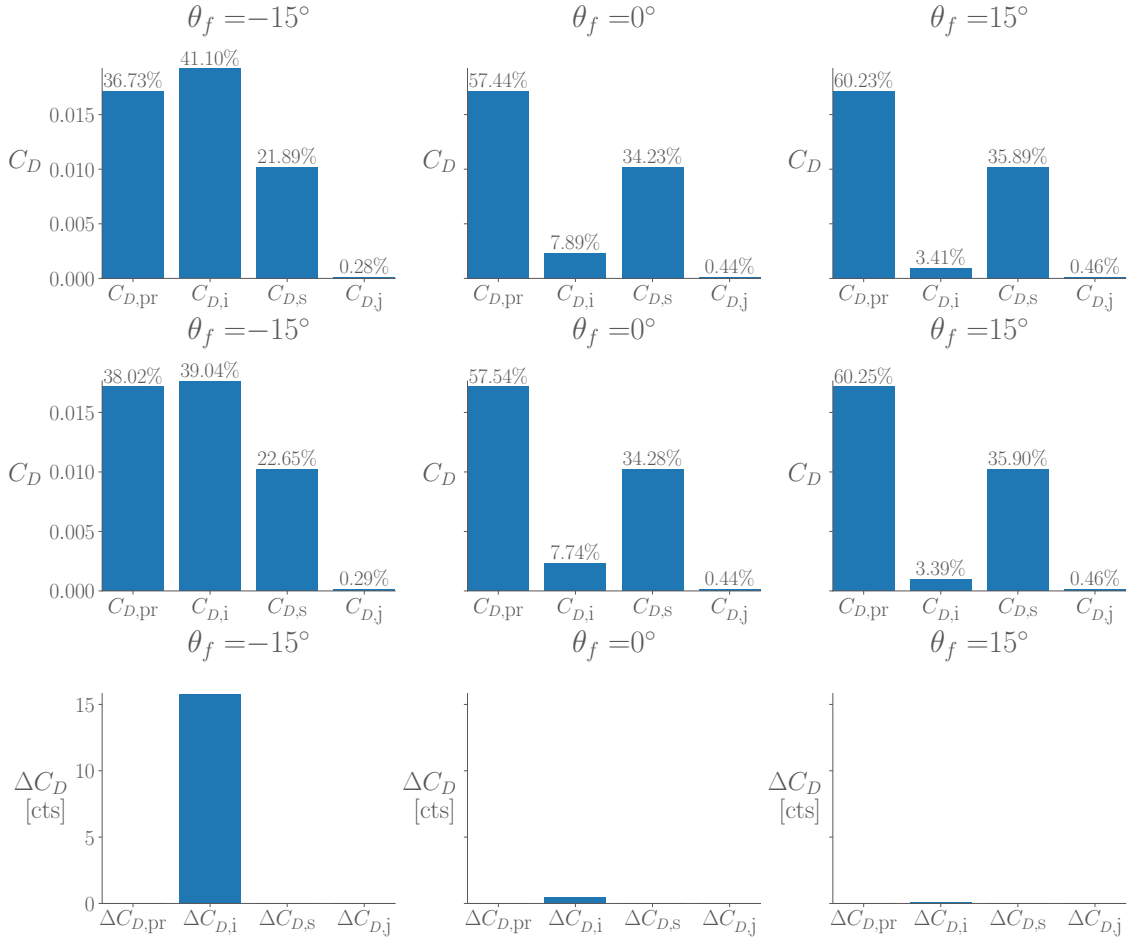

Figure 6: Drag build-up for different fiber angles with no free-surface effect (top row) and with free-surface effect (middle) at $U_\infty = 18$ m/s. Drag deltas between no free-surface and free-surface given in drag counts (bottom).

As a final exploration into the performance, we run polars by varying the wing mounting rake α_r from $-5°$ to $15°$ in $0.5°$ steps. This could correspond to a rake control mechanism or a designer choice. The polars are in Figure 7 where dashed lines are with the free surface model. We add a rigid hydrofoil case as well to see if tailored flexibility offers performance gains. There are some experimental results from Ashworth Briggs (2018, Sec. 6.4.1) for a pitching polar (not wing mounting rake) at $Re = 0.48 \times 10^6$ and $U_\infty = 4$ m/s, which is a very different flow condition; however, we plot them as a comparison to have a general idea of the polar trends. The overall bucket shape comparisons will not be entirely fair because (1) the simulations are at a high enough speed where structural deflections occur and influence drag, whereas the experiment can be assumed to have mostly rigid T-foil hydrodynamics, (2) the angle of attack here is base rake whereas the experiment varied overall pitch, and (3) laminar flow existed in the experiment but our empirical model assumes fully turbulent flow. Nevertheless, we can look at the $\alpha = 0°$ cases between experiment and simulation and draw some parallels.

As expected, the simulated polars are symmetric about $C_L = 0$ and $\alpha_r = 0°$ because of the uncambered hydrofoil section. All T-foils have the same $C_{D,\min} = 275$ drag counts at the $C_L = 0$ condition corresponding to the same parasitic drag. The
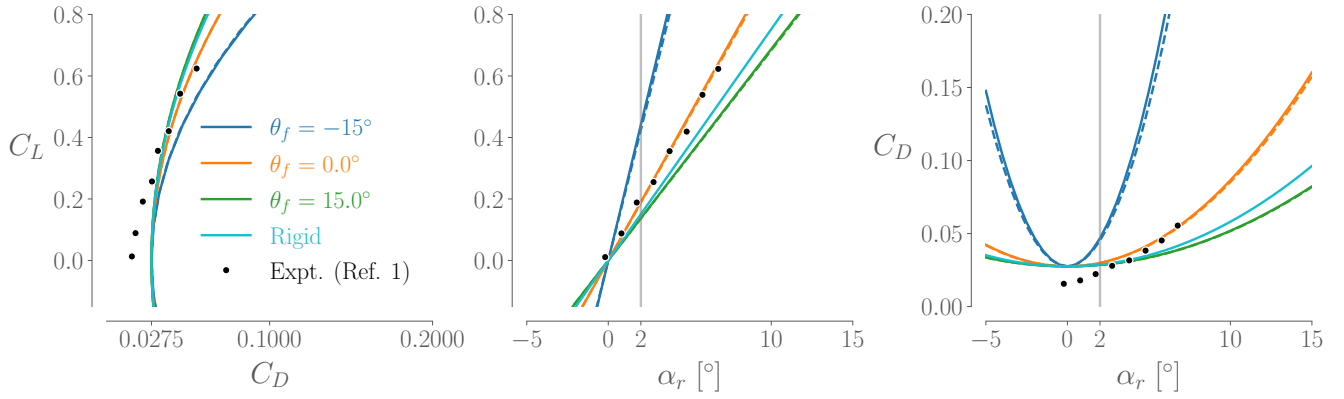
Figure 7: Performance polars of T-foils for $U_\infty = 18\,\text{m/s}$ varying base rake. Solid lines are no free surface and dashed are with the free surface model. The experimental results varied strut rake.

$C_L = 0$ drag value is slightly higher than the experimental $C_{D,\text{min}}$, but this could be a combined effect of inaccurate spray drag, junction intersection drag, and skin friction drag because of the mismatched Reynolds and Froude numbers between experiment and simulation. The experiment had laminar flow at low angles of attack (Binns et al., 2008) while we assumed turbulent flow in the ITTC 1957 line. Future work may warrant an improved parasitic drag model accounting for these effects to accurately assess drag trades.

The more positive fiber angle foils have wider drag buckets, indicating that the max L/D would be best for the $\theta_f = 15°$ T-foil. This would suggest that the $\theta_f = 15°$ T-foil is able to maintain a spanwise lift distribution closer to elliptical across angles of attack and thus reduce the lift-induced drag. This hydrofoil even outperforms the rigid hydrofoil, though not noticeably until much higher C_L and α_r. The polar makes sense because the $\theta_f = 0°$ has positive tip twist (see Figure 4) with increasing lift, but the $\theta_f = 15°$ has washout at the tips from the nose-down bend-twist coupling. The $\theta_f = 0°$ T-foil would therefore have too much load outboard. Lastly, since the lifting line model is potential flow, we do not capture the stalling effect at higher α_r so we should actually see a precipitous drop-off in C_L in the polars at higher angles. Based on these results, the $\theta_f = 15°$ seems to be the best-performing T-foil of the studied configurations, indicating that a designer should look in the direction of more positive fiber angle composite T-foils that promote washout at higher lift.

CONCLUSIONS

Through simple structural and hydrodynamic models, we explored the influence of free-surface effects and material anisotropy on the static hydroelastic response of a composite T-foil. We explored the hydrostructural performance of three composite T-foils, each with different fiber angles.

Negative fiber angles produce more outboard lift and moment, resulting in more outboard deflections with nose-up tip twist. This behavior is bad for both hydrodynamics and structures because of increased cavitation, ventilation, and tip stall susceptibility as well as material failure risk. Zero or positive fiber angles are better for load alleviation because there is more tendency towards washout via nose-down bend-twist coupling. The more positive fiber angle T-foils had better drag polars because of the lower lift-induced drag. We deduce that these types of composite T-foils tend to be hydrodynamically and structurally better, at least for the given initial geometry.

The free surface model used here assumes infinite Froude number and reduced all lift and moments (and hence deflections) on the T-foils. In the cases studied, lift-induced drag dominated, so the free surface also reduced drag because of the reduced lift. The effect was minor because of low depth-to-chord ratio, though further studies into heel or cant angle would be interesting to see the asymmetric loading effect on the flexible composite structure.

In a more sophisticated hydrodynamics lifting line model, finite Froude number effects would more accurately model the bound vorticity (γ) on the foil than the infinite Froude number assumption. This would then enable more accurate lift-induced drag and wave drag estimates that depend on vorticity. The accuracy across finite Froude numbers will be important for higher fidelity design optimizations that may tune submergence depth and chord of hydrofoils if they were design variables, which both affect Froude number. A possible future avenue for considering free-surface effects that balances accuracy and cost is the desingularized Rankine-source panel method with a body-exact, linearized free-surface condition (Cao et al., 1991).

Overall, material anisotropy offers potential for customized spanwise loading of T-foils, which is important for control surface effectiveness, hydrodynamic efficiency through lower drag, and structural efficiency through less/more effective material usage. The models presented here are a computationally cheap way to evaluate preliminary composite foil designs whilst capturing the necessary fluid-structure interactions present in high-speed surface craft design. Our results also show expected and consistent trends with previous numerical and experimental work that verifies the current toolset for rapid, conceptual, design space exploration of more complicated marine appendage geometries. Future work could consider a Froude number-dependent free surface model, coupling of T-foil deflections to vessel dynamics, or unsteady analyses to capture the vessel response in waves.

CONTRIBUTION STATEMENT

Galen W. Ng: Methodology, Software, Formal analysis, Conceptualization, Data curation, Writing – original draft. **Eirikur Jonsson:** Supervision, Methodology, Writing – review and editing. **Yingqian Liao:** Supervision, Methodology, Writing – review and editing. **Sicheng He:** Supervision, Methodology, Writing – review and editing. **Joaquim R.R.A. Martins:** Supervision, Resources, Writing – review and editing.

ACKNOWLEDGEMENTS

REFERENCES

Ashworth Briggs, A. J. E. (2018). *Free surface interaction of a ' T-foil ' hydrofoil*. PhD thesis, University of Tasmania.

Beck, R. F. and Reed, A. M. (2001). Modern computational methods for ships in a seaway. *Transactions of Society of Naval Architects and Marine Engineers*, 109:1–51.

Binns, J. R., Brandner, P. A., and Plouhinec, J. (2008). The effect of heel angle and free-surface proximity on the performance and strut wake of a moth sailing dinghy rudder T-foil. In *Proceedings of the 3rd High Performance Yacht Design Conference*, Auckland, NZ.

Brennen, C. E., editor (2014). *Cavitation and bubble dynamics*. Cambridge University Press.

Cao, Y., Schultz, W. W., and Beck, R. F. (1991). Three-dimensional desingularized boundary integral methods for potential problems. *International Journal for Numerical Methods in Fluids*, 12(8):785–803.

Carlton, J. (2018). *Marine Propellers and Propulsion*. Butterworth-Heinemann.

Chapman, R. B. (1971). *Spray drag of surface-piercing struts*, volume 251. Naval Undersea Research and Development Center.

Damley-Strnad, A., Harwood, C. M., and Young, Y. L. (2019). Hydrodynamic performance and hysteresis response of hydrofoils in ventilated flows. In *Sixth International Symposium on Marine Propulsors*, Rome, Italy.

Faltinsen, O. M. (2006). *Hydrodynamics of high-speed marine vehicles*. Cambridge University Press.

Faye, A., Perali, P., Augier, B., Sacher, M., Leroux, J.-B., Nême, A., and Astolfi, J.-A. (2024). Fluid-structure interactions response of a composite hydrofoil modelled with 1d beam finite elements. *Journal of Sailing Technology*, 9(01):19–41.

Glauert, H. (1983). *The Elements of Aerofoil and Airscrew Theory*. Cambridge Science Classics. Cambridge University Press.

Godø, J. M. K. and Steen, S. (2023a). A comparative study of the energy efficiency of hydrofoil vessels and slender catamarans. In *HSMV 2023: Proceedings of the 13th Symposium on High Speed Marine Vehicles*, volume 7, pages 159–171.

Godø, J. M. K. and Steen, S. (2023b). An efficient method for unsteady hydrofoil simulations, based on non-linear dynamic lifting line theory. *Ocean Engineering*, 288:116001.

Groo, L., Steinke, K., Inman, D. J., and Sodano, H. A. (2019). Vibration damping mechanism of fiber-reinforced composites with integrated piezoelectric nanowires. *ACS Applied Materials and Interfaces*, 11(50):47373–47381.

Hoerner, S. F. (1965). *Fluid-Dynamic Drag*. Hoerner Fluid Dynamics, Bakersfield, CA.

Kroo, I. M. (2001). Drag due to lift: Concepts for prediction and reduction. *Annual Review of Fluid Mechanics*, 33:587–617.

Liao, Y., Martins, J. R. R. A., and Young, Y. L. (2021). 3-D high-fidelity hydrostructural optimization of cavitation-free composite lifting surfaces. *Composite Structures*, 268:113937.

Liao, Y., Martins, J. R. R. A., and Young, Y. L. (2023). Hydrostructural optimization of single-layer and multi-layer composite lifting surfaces. *Composite Structures*, 307:116650.

Liao, Y., Yildirim, A., Martins, J. R. R. A., and Young, Y. L. (2022). RANS-based optimization of a T-shaped hydrofoil considering junction design. *Ocean Engineering*, 262:112051.

Maung, P. T., Prusty, B. G., Donough, M. J., Oromiehie, E., Phillips, A. W., and St John, N. A. (2023). Automated manufacture of optimised shape-adaptive composite hydrofoils with curvilinear fibre paths for improved bend-twist performance. *Marine Structures*, 87:103327.

Mulcahy, M. L., Croaker, P., McGuckin, D. G., Brandner, P. A., and Kississoglou, N. (2014). Optimisation applied to composite marine propeller noise. In *INTER-NOISE and NOISE-CON Congress and Conference Proceedings*, volume 249, pages 4012–4019. Institute of Noise Control Engineering.

Newman, J. N. (2018). *Marine hydrodynamics*. The MIT press.

Ng, G. W., Jonsson, E., He, S., and Martins, J. R. R. A. (2023). Coupled strip theory and finite element method for stability analysis of composite hydrofoils. In *Proceedings of the 6th International Conference on Innovation in High Performance Sailing Yachts and Wind-Assisted Ships*, Lorient, France.

Ng, G. W., Martins, J. R. R. A., and Young, Y. L. (2022). Optimizing steady and dynamic hydroelastic performance of composite foils with low-order models. *Composite Structures*, 301:116101.

Nicolas, H., Perali, P., Sacher, M., and Bot, P. (2023). Boundary element method analysis of 3d effects and free-surface proximity on hydrofoil lift and drag coefficients in varied operating conditions. *Journal of Sailing Technology*, 8(01):183–199.

Raymer, D. P. (2012). *Aircraft Design: A Conceptual Approach*. AIAA, Reston, VA, 5th edition.

Simpson, R. L. (2001). Junction flows. *Annual Review of Fluid Mechanics*.

Torenbeek, E. (1990). *Synthesis of Subsonic Airplane Design*. Delft University Press and Kluwer Academic Publishers, 6th edition.

Yamatogi, T., Murayama, H., Uzawa, K., Kageyama, K., and Watanabe, N. (2009). Study on cavitation erosion of composite materials for marine propeller. In *The 17th International Conference on Composites (ICCM-17)*, Edinburgh, UK.

Young, Y. L., Harwood, C. M., Montero, M. F., Ward, J. C., and Ceccio, S. L. (2017). Ventilation of lifting bodies: Review of the physics and discussion of scaling effects. *Applied Mechanics Reviews*, 69(1):010801.